^{27}Al NMR insight into the phase transition in $BaFe_2Al_9$

C. Y. Huang,[1] H. Y. Lee,[1,2] Y. C. Chang,[1] Chon Kit Hong,[1] Y. R. Ou,[1,2] C. N. Kuo,[1,3,*] and C. S. Lue[1,2,3,†]

[1]*Department of Physics, National Cheng Kung University, Tainan 70101, Taiwan*

[2]*Program on Key Materials, Academy of Innovative Semiconductor and Sustainable Manufacturing, National Cheng Kung University, Tainan 70101, Taiwan*

[3]*Taiwan Consortium of Emergent Crystalline Materials, National Science and Technology Council, Taipei 10601, Taiwan*

(Received 6 September 2021; accepted 24 October 2022; published 1 November 2022)

We have applied ^{27}Al nuclear magnetic resonance (NMR) spectroscopy to investigate the iron-based aluminide of $BaFe_2Al_9$. This material has been a subject of current interest due to indications of charge density wave behavior below the transition temperature $T_C \simeq 100$ K. Two sets of the ^{27}Al NMR resonance lines that are associated with two nonequivalent crystallographic aluminum sites have been well resolved. We have discussed the obtained electric field gradient and anisotropic Knight shift for each individual aluminum site, revealing the strong *ab* plane bonding configuration for the structural properties of $BaFe_2Al_9$. Pronounced features in the isotropic Knight shift and nuclear spin-lattice relaxation rate have been observed in the vicinity of T_C. Furthermore, the detailed ^{27}Al NMR analyses have provided evidence for the decrease of the electronic density of states upon lowering temperature below T_C.

DOI: 10.1103/PhysRevB.106.195101

I. INTRODUCTION

Very recently, the ternary aluminide of $BaFe_2Al_9$ was reported to exhibit a first-order phase transition at $T_C \simeq 100$ K [1]. The first-order transition has been characterized by the thermal hysteresis with the transition width of about 10 K from the magnetic susceptibility measurement. Notably, the temperature-dependent susceptibility shows a sudden drop in the vicinity of T_C, bearing a resemblance to those observed in the charge density wave (CDW) systems such as $Lu_5Rh_4Si_{10}$, $Lu_2Ir_3Si_5$, and CsV_3Sb_5 [2–6]. The results of the powder x-ray diffraction (XRD) and neutron diffraction have revealed an abrupt change of the lattice parameters with about 0.5% increase in the lattice constant a and 1.5% shrinkage in c undergoing the phase transition. From the refinement of the neutron diffraction data, the substantial change in Fe and Ba atomic displacement parameters upon cooling through T_C has been unveiled. Furthermore, additional superlattice peaks indicating the structural modulation have been resolved from the low-temperature single-crystal XRD. These peaks determined at 70 K have been indexed by three wave vectors: $(0.5, 0, q_z)$, $(0.5, 0.5, q_z)$, and $(0, -0.5, q_z)$ with $q_z \simeq 0.3$. With these respects, a scenario which shows modulated displacements at the Fe atoms along the c-axis direction has been proposed to be responsible for the CDW ordering in $BaFe_2Al_9$ [1].

$BaFe_2Al_9$ adopts the three-dimensional (3D) hexagonal $BaFe_2Al_9$-type structure (space group $P6/mmm$) [1,7–9]. As illustrated in Fig. 1, the barium atoms occupy the $1a$ site and the iron atoms reside at the $2c$ site (in Wyckoff notations). There are two nonequivalent crystallographic aluminum sites, termed as Al(1) and Al(2), respectively. Each Al(1) atom resides at the $3f$ site and each Al(2) atom at the $6m$ site. The aluminum substructure can be viewed as a 3D network of vertex-sharing octahedra connected by four Al(2) atoms and two Al(1) atoms at the vertices. These octahedra form a kagome structure in the *ab* plane. Each barium atom in the hexagon is bridged by six Al(2) atoms, while the iron atom in the center of the trigonal prism is bridged by three Al(1) atoms. The latter gives rise to the shortest Fe-Al(1) bond with the bond length of 2.32 Å along the *ab* plane, and the former yields a longer Fe-Al(2) distance of 2.58 Å with an oblique bonding direction to the *ab* plane [7,8]. According to the previously proposed model [1], the aforementioned CDW is localized on the chain of the Fe atoms separated by the distorted Ba chains along the c axis. Furthermore, the possible CDW ground state is driven by the filling of the Fe d orbitals with capturing electrons from the surrounding Al atoms.

Nuclear magnetic resonance (NMR) measurement is a local probe to explore the atomic structure and electronic properties of the selected crystallographic site [10–21]. Various CDW systems such as $NbSe_3$, $LaPt_2Ge_2$, and CsV_3Sb_5 have been widely investigated by means of NMR spectroscopy [22–26]. Recently, a magnetic field induced CDW behavior has been observed in single-layered $Bi_2Sr_{2-x}La_xCuO_6$, demonstrating the usefulness of NMR experiments for CDW research [27]. In this study, we have carried out the ^{27}Al NMR measurement on $BaFe_2Al_9$ to examine the changes of structural and electronic properties at each individual aluminum site accompanied by the phase transition. A comparison of the results between Al(1) and Al(2) sites would provide experimental insights into the underlying mechanisms of the phase transition.

*Corresponding author: kuochianung@gmail.com
†Corresponding author: cslue@mail.ncku.edu.tw

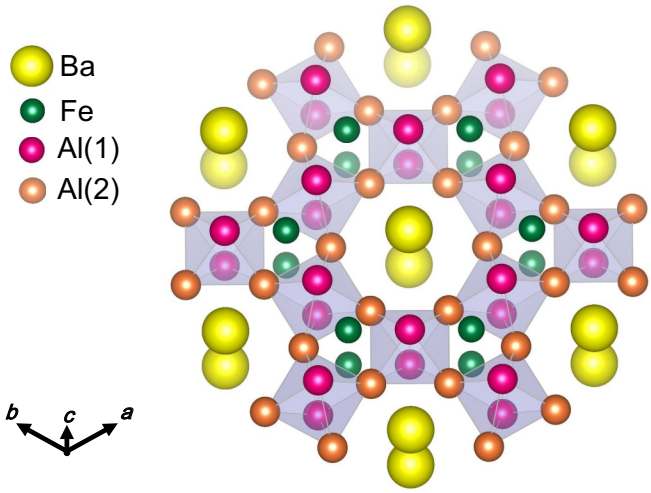

FIG. 1. Crystal structure of $BaFe_2Al_9$.

II. EXPERIMENT RESULTS AND DISCUSSION

Single crystals of $BaFe_2Al_9$ were grown in Al self-flux. The mixtures of Ba pieces, Fe powder, and Al ingots with the molar ratio of Ba:Fe:Al = 6 : 8 : 85 were placed in an alumina crucible and sealed in a silica tube with partial argon. The ampoule was heated with a heating rate of 50 K/h up to 1373 K and then kept at this temperature for 12 h, followed by cooling down to 1173 K for 100 h. Several rodlike crystals of about 4 mm in length and 1.5 mm in diameter, with metallic luster, were separated from the molten Al flux by centrifugation. The remaining Al drops on the crystal surfaces were etched in 1% HCl solution for 1 wk. Figure 2 shows the room-temperature single-crystal XRD with the diffraction peaks indexed to the expected $P6/mmm$ phase of $BaFe_2Al_9$. The determined lattice parameter $a = b = 8.02 \pm 0.005$ Å is close to those reported in the literature [1,7,8]. The Laue diffraction pattern of single-crystalline $BaFe_2Al_9$ along the (010) direction is displayed in the inset of Fig. 2. Good crystallization of our crystal is confirmed by the sharp spots in the observed Laue pattern.

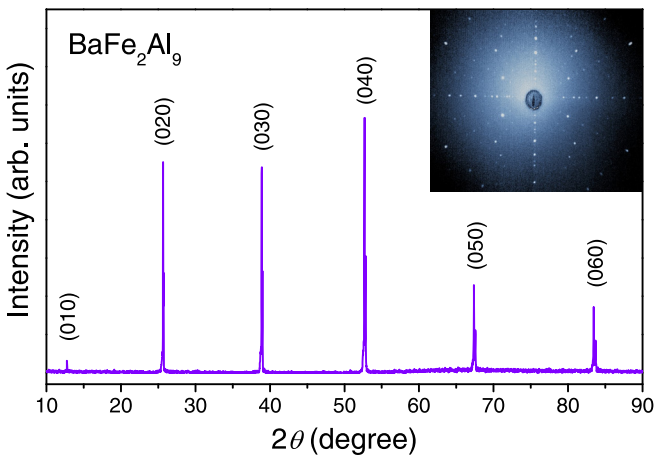

FIG. 2. Single-crystal x-ray diffraction of the $(0l0)$ planes measured at room temperature. The inset shows a photograph of the Laue diffraction pattern of $BaFe_2Al_9$.

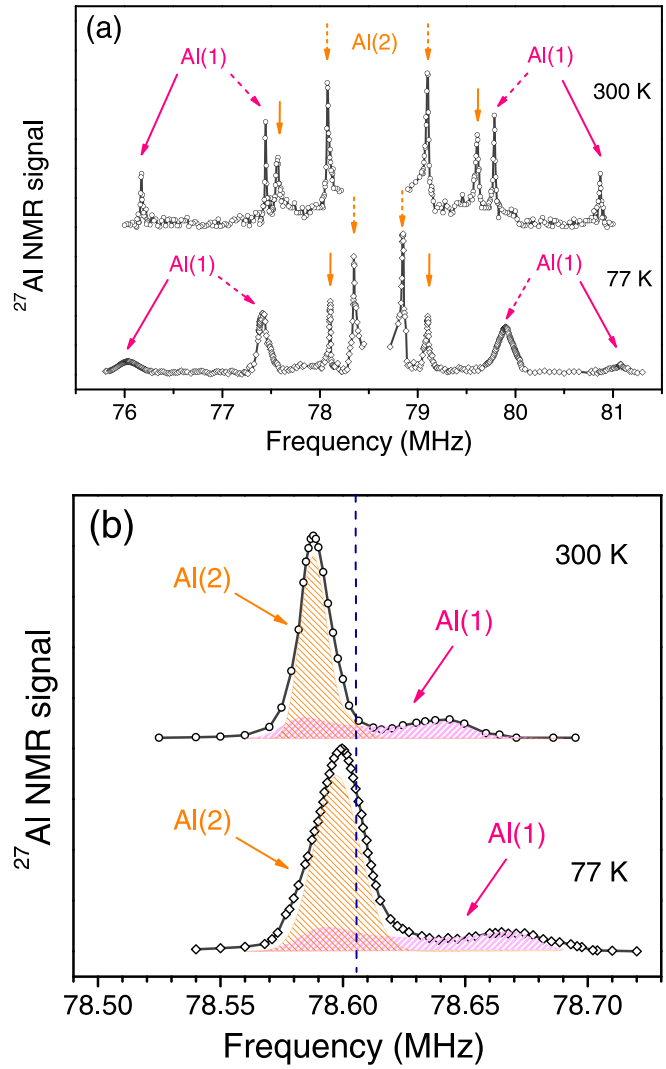

FIG. 3. (a) ^{27}Al NMR satellite lines of $BaFe_2Al_9$ measured at 300 and 77 K. For each Al site, the corresponding $\pm\frac{1}{2} \leftrightarrow \pm\frac{3}{2}$ and $\pm\frac{3}{2} \leftrightarrow \pm\frac{5}{2}$ transitions are marked by the dashed and solid arrows, respectively. (b) ^{27}Al NMR central transition lines of $BaFe_2Al_9$ at 300 and 77 K, respectively. The dashed vertical line denotes the position of the ^{27}Al reference frequency. The simulated curve for each Al site is depicted as described in the text.

NMR measurements were carried out under a constant field of 7.08 T. The powdered specimen obtained from crushed crystals was used since the chunky crystal of $BaFe_2Al_9$ shatters accompanied by the structural phase transition. The ^{27}Al NMR frequency shift refers to the ^{27}Al resonance frequency of aqueous $AlCl_3$. Since the crystallographic symmetry at the Al(1) and Al(2) sites is not cubic, the quadrupole nucleus ^{27}Al (nuclear spin $I = 5/2$) coupled with the electric field gradient (EFG) would lead to five NMR resonance lines per site. For $BaFe_2Al_9$, ten transition lines associated with two Al sites have been well resolved. In addition to the central transition lines $(-\frac{1}{2} \leftrightarrow +\frac{1}{2})$, which are displayed separately in Fig. 3(b), the remaining eight satellite lines are demonstrated in Fig. 3(a). For a powdered specimen, these lines exhibit as a typical powder pattern, with distinctive edge features corresponding to the quadrupole parameters. The four

TABLE I. Quadrupole frequency and isotropic and anisotropic Knight shifts for each of the Al sites obtained at 300 and 77 K, respectively.

Site	ν_Q (MHz)	$K_{\rm iso}$ (ppm)	K_{an} (ppm)
Al(1) 300 K	2.34 ± 0.02	320 ± 30	540 ± 50
77 K	2.53 ± 0.03	570 ± 50	400 ± 50
Al(2) 300 K	1.02 ± 0.005	− 190 ± 20	200 ± 20
77 K	0.495 ± 0.005	− 90 ± 25	130 ± 20

edge singularities for each Al site arising from the $\pm\frac{1}{2} \leftrightarrow \pm\frac{3}{2}$ (dashed arrows) and $\pm\frac{3}{2} \leftrightarrow \pm\frac{5}{2}$ (solid arrows) transitions were marked. The site identification for these satellite lines is based on the line splitting referring to the corresponding central transition line given in Fig. 3(b), obtained by the line-shape analysis described later.

Since the first-order quadrupole interaction is the main effect shaping the satellite lines, the corresponding quadrupole frequency, ν_Q, was determined directly from the separation of these lines. Results were tabulated in Table I. Here $\nu_Q = 3eQV_{zz}/[2I(I+1)h]$ is defined by the nuclear quadrupole moment Q and the largest principal axis component of the EFG tensor of V_{zz}. In principle, the noncubic arrangement of the charged lattice ions (lattice EFG) and the nonuniform charge density of the valence electrons (valence EFG) are common origins responsible for the observed quadrupole interaction. For $BaFe_2Al_9$, the short Fe-Al bonds indicate that the bonding may have a covalent character [7,8]. This is in agreement with the assignment of a larger ν_Q to the Al(1) site, attributed to a concentration of the bonding charge in the *ab* plane. The hybridization between the Al *p* and the Fe *d* orbitals should play an important role due to the corresponding covalent charges bond in this plane. The fact that the Fe-Al(2) distance is longer and bonds obliquely to the *ab* plane is also consistent with a smaller ν_Q assigned to the Al(2) site. Hence, the comparison of ν_Q for each individual Al site gives a microscopic picture for the strong directional bonding of the structural properties, being consistent with the brittleness in $BaFe_2Al_9$ [1]. Upon cooling, ν_Q for the Al(1) site increases slightly from 2.34 at room temperature to 2.53 MHz at 77 K while ν_Q for the Al(2) site reduces drastically from 1.02 to 0.495 MHz. Apparently, the observation can be simply ascribed to the change of the valence charges. To some extent, this is a manifestation of the lattice distortion with abrupt compression along the *c* direction and expansion in the *ab* plane.

Figure 3(b) shows two representative central transition spectra taken at 300 and 77 K, respectively. Each spectrum is complicated because of the simultaneous presence of quadrupole and anisotropic Knight-shift effects. In $BaFe_2Al_9$, the ^{27}Al quadrupole shift and the angle-dependent Knight shift are axially symmetric for both Al(1) and Al(2) sites. Therefore, the frequency shift of the central transition line for each aluminum site, $\Delta\nu$, to the second-order quadrupole interaction and anisotropic Knight shift is

$$\frac{\Delta\nu}{\nu_o} = \frac{K_{an}}{2(1+K_{\rm iso})}(3\cos^2\theta - 1) + \frac{1}{2}\left(\frac{\nu_Q}{\nu_o}\right)^2(1-\cos^2\theta)(1-9\cos^2\theta). \quad (1)$$

Here ν_o is the Larmor frequency, $K_{\rm iso}$ the isotropic Knight shift, K_{an} the anisotropic Knight shift, and θ the angle between the crystal symmetry axis and the external magnetic field. The line-shape function was simulated, following Cohen and Reif [28]:

$$P(\nu-\nu_o) = \frac{1}{2}\left|\frac{d\nu}{d\cos\theta}\right|^{-1}. \quad (2)$$

By substituting the determined ν_Q's and tuning K_{an}, the positions of shoulders and singularities of the NMR spectrum can be found. The best-fit curves, evaluated by eye, are depicted in Fig. 3(b). The corresponding values for $K_{\rm iso}$ and K_{an} were thus obtained with the results listed in Table I. Note that in these fits we constrained the line-shape areas for the Al(1) and Al(2) sites by the 1 to 2 ratio according to their occupations in the $BaFe_2Al_9$-type crystallographic structure. Accordingly, the splitting feature of the central transition line for the Al(1) site has been identified, and the peak at the low-frequency side has been found to be governed by the Al(2) site.

The anisotropic Knight shift mainly arises from two terms: the spin dipolar interaction and the paramagnetic (orbital) shift. Important contributions for the latter will come from local Al-*p* orbitals as well as *d* orbitals from neighboring Fe sites. In an environment of axial symmetry as for the present case of $BaFe_2Al_9$, K_{an} is equal to $\frac{2}{3}(K_c - K_{ab})$, with K_c and K_{ab} corresponding to the Knight shifts in the *c* direction and the *ab* plane, respectively. Therefore, a larger K_{an} for the Al(1) site indicates the strong directionality in the valence charge distribution. Such a result is consistent with the large EFG, revealed from a larger ν_Q for the Al(1) site. As mentioned above, local Al-*p* orbital electrons also contribute to K_{an}. In fact, the decrease in K_{an} for both Al sites observed at 77 K should originate from this mechanism. It implies a significant charge reduction and/or less inhomogeneous charge distribution undergoing the phase transition below $T_C \simeq 100$ K. Such a result agrees with the previously proposed model that the filling of the Fe *d* orbitals with accepting the electrons from the neighboring Al atoms plays an essential role for approaching the ground state in $BaFe_2Al_9$ [1]. As a consequence, it changes the Al bonding and develops a huge mechanical strain, leading to the shattering of the $BaFe_2Al_9$ crystal undergoing the structural phase transition.

The isotropic Knight shift can be decomposed into three parts as $K_{\rm iso} = K_s + K_{\rm orb} + K_{sd}$. The first term arises from the Al *s*-contact electrons which is related to the *s*-character Fermi-level density of states (DOS). The second one, $K_{\rm orb}$, is the orbital shift due to the contribution from the Van Vleck orbital magnetism. It is noticeable that the effect arising from the Al 3*p* electrons can be neglected, owing to the relatively weak core polarization from *p* orbitals [29]. The third term, K_{sd}, reflects the polarization of Al-*s* electrons by the 3*d* spins from Fe through the transferred hyperfine interaction which could be either positive or negative depending on the polarization by the transferred hyperfine field [30]. We here confirmed that negative K_{sd} for the Al(2) site overcomes the contribution from K_s and $K_{\rm orb}$, leading to negative values of $K_{\rm iso}$ within the measured temperature range. It is worthwhile mentioning that negative Knight shifts have been reported in various transition-metal-based aluminides such as Al_3V,

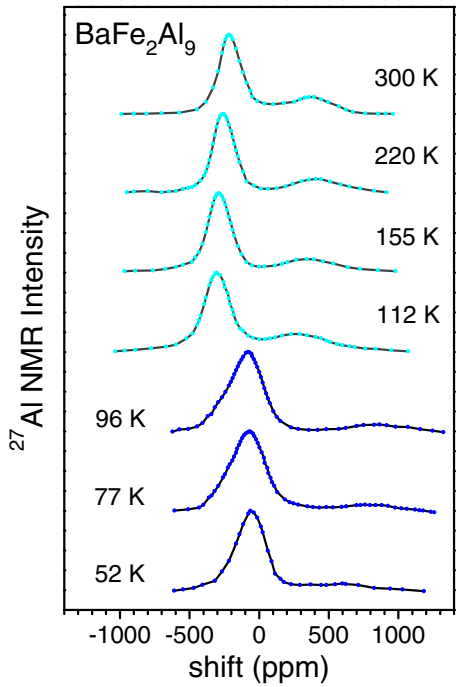

FIG. 4. Evolution of ^{27}Al NMR central transition lines of $BaFe_2Al_9$ measured above and below the phase transition temperature $T_C \simeq 100$ K.

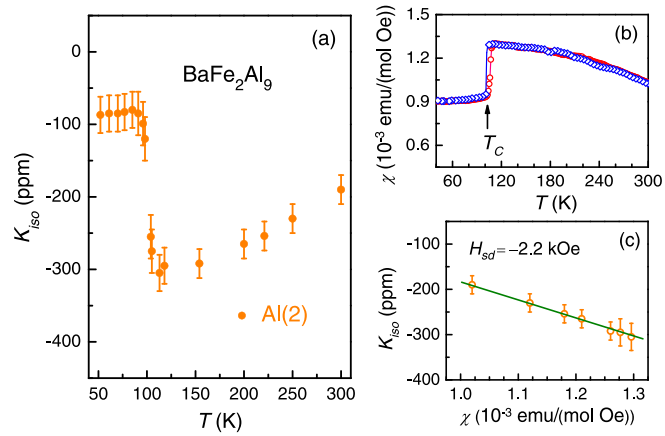

FIG. 5. (a) Temperature dependence of the ^{27}Al NMR isotropic Knight shift for the Al(2) site of $BaFe_2Al_9$. (b) Magnetic susceptibility data obtained under a constant field of 1 T. (c) Variation of K_{iso} versus χ for the Al(2) site of $BaFe_2Al_9$. The straight line indicates the linear relationship and the corresponding slope yields the transferred hyperfine field.

FeAl, $FeAl_2$, Fe_4Al_{13}, and Cr_2AlC [10,31–35]. In contrast, the sign of K_{iso} is positive for the Al(1) site. We argue that the positive shift is not dominated by K_s since the observed Korringa behavior in the spin-lattice relaxation rate indicated a small s-character DOS at the Fermi level. In this respect, most of the positive K_{iso} would originate from K_{orb}. It is noteworthy that the effect of K_{sd} for the Al(1) site is expected to be more substantial than that for the Al(2) site due to the stronger Fe-Al(1) interaction in $BaFe_2Al_9$. Nevertheless, the contribution from K_{orb} for the Al(1) site is still greater than that from K_{sd}, resulting in positive K_{iso} as observed.

To gain more insight into the evolution of the central transition lines across the phase transition, we display several representative spectra measured between 52 and 300 K in Fig. 4. Upon cooling below T_C, the entire spectrum shifts abruptly to higher frequencies, indicative of drastic changes in the electronic states along with the phase transition. However, the width of the transition lines slightly increases with lowering temperature. As a matter of fact, the simulated curves for both Al sites exhibit a weak broadening at 77 K, as illustrated in Fig. 3(b). Such an observation provides evidence that the phase transition is not likely due to the magnetic ordering, in which an extremely broad spectrum accompanied by a huge frequency shift in the transition lines should take place.

We have found that the value of K_{iso} for the Al(2) site is close to the frequency shift measured from the position of the maximum intensity of the central transition line. It is thus realistic to estimate K_{iso} directly from the maximum of the peak for each temperature. With this accordance, the temperature variation of K_{iso} for the Al(2) site of $BaFe_2Al_9$ is presented in Fig. 5(a). Above T_C, K_{iso} decreases with lowering temperature, opposite to the trend in the magnetic susceptibility χ which is given in Fig. 5(b). The relation between K_{iso} and χ can be correlated as

$$K_{iso} = K_o + \frac{H_{sd}}{N_A \mu_B}\chi. \tag{3}$$

Here K_o is the temperature-independent shift, N_A is the Avogadro constant, μ_B is the Bohr magneton, and H_{sd} is the transferred hyperfine field from the Fe $3d$ spins sensed by the Al nucleus. The Clogston-Jaccarino plot [36] that shows the linear relation between K_{iso} vs χ of $BaFe_2Al_9$ is presented in Fig. 5(c). From the corresponding slope, we extracted $H_{sd} = -2.2 \pm 0.4$ kOe for the Al(2) site. It is worthwhile mentioning that a similar value of -2.4 kOe was found in Al_3V [31] while a bit larger field of -3.5 kOe was reported in $FeAl_2$ [33].

While the result of the Knight shift reveals the static electronic feature, the nuclear spin-lattice relaxation time T_1 is a local probe of dynamic behavior of the electrons. The T_1 measurements were carried out using an inverse recovery method. We found T_1 by centering the transmission frequency at the peak position of the central transition line and recorded the signal strength by integrating the recovered spin-echo signal. In this experiment, the relaxation process involves adjacent pairs of spin levels, and the corresponding spin-lattice relaxation is a multiexponential expression [37]. For the central transition with $I = 5/2$, the recovery of the nuclear magnetization follows:

$$\frac{M(t) - M(\infty)}{M(\infty)} = -2\alpha(0.257e^{-t/T_1} + 0.267e^{-6t/T_1} + 0.476e^{-15t/T_1}). \tag{4}$$

Here $M(t)$ is the magnetization at the recovery time t and $M(\infty)$ is the magnetization after long-time recovery. The parameter α is a fractional value derived from the initial conditions used in our experiment. Our T_1 values were thus obtained by fitting to this multiexponential recovery function.

The temperature variation of the nuclear spin-lattice relaxation rate T_1^{-1} for $BaFe_2Al_9$ is shown in Fig. 6. The presence

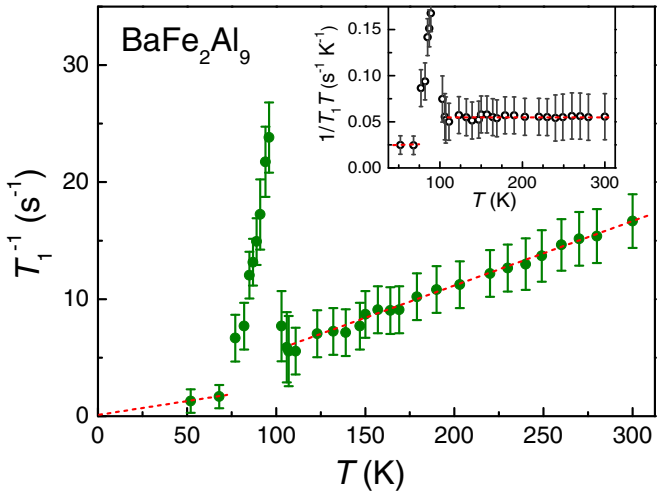

FIG. 6. Temperature dependence of T_1^{-1} for $BaFe_2Al_9$. Each dashed line indicates the Korringa behavior with different slope. Inset: Temperature variation of $1/T_1T$, showing a constant value of about 0.055 s^{-1} K^{-1} for $T > T_C$ and 0.025 s^{-1} K^{-1} for $T < T_C$.

of a peak in T_1^{-1} clearly manifests an intrinsic phase transition at around 100 K. Since the phase transition is not accounted for by the magnetic origin, the observed peak cannot be interpreted as the result of the rapid fluctuations of the spin dynamics arising from magnetic ordering. While the mechanism responsible for the increase in the ^{27}Al NMR relaxation rate remains unclear, the peak feature behaves quite similarly to those observed in the vicinity of the phase transitions of the CDW material $NbSe_3$ and CDW candidate $La_3Co_4Sn_{13}$ [38,39].

Apart from the transition region, the data of T_1^{-1} obey the Korringa behavior (constant T_1T) [40], suggesting that the conduction electrons are responsible for the observed relaxation mechanism. For clarity, a plot of $1/T_1T$ vs T is given in the inset of Fig. 6. From the magnitude of $1/T_1T$, one can evaluate the Al 3*s* partial Fermi-level DOS within the model of the noninteracting electrons:

$$\left(\frac{1}{T_1T}\right) = 2hk_B\left[\gamma_n H_{hf}^s N_s(E_F)\right]^2. \quad (5)$$

Here h, k_B, and γ_n are the Plank constant, the Boltzmann constant, and the Al nuclear gyromagnetic ratio, respectively. $N_s(E_F)$ is the partial DOS at the Fermi-level E_F in the unit of states/eV per spin, and H_{hf}^s represents the hyperfine field per spin of the Al 3*s* electrons. Taking $H_{hf}^s \simeq 1.9 \times 10^3$ kOe in Al-based metals [10,12,29,35,41–43], we extracted $N_s(E_F) \simeq 0.028$ states/eV per atom from Eq. (5) with the experimental value of $1/T_1T \simeq 0.055\ s^{-1}\ K^{-1}$ for $T > T_C$. Similarly, $N_s(E_F) \simeq 0.019$ states/eV was obtained from $1/T_1T \simeq 0.025\ s^{-1}\ K^{-1}$ for $T < T_C$. With this accordance, about 32% loss in $N_s(E_F)$ associated with the phase transition has been estimated. The marked reduction in $N_s(E_F)$ at low temperatures is consistent with the scenario of the Fermi-surface nesting associated with CDW ordering. It should be noted that we could not separate T_1^{-1} from each individual site since two Al NMR central transition lines are intrinsically mixed, as seen from Fig. 3(b). Therefore the presented T_1^{-1} is the mixture of the contribution from both Al(1) and Al(2) sites, and the deduced $N_s(E_F)$ would be the average result from two Al sites.

III. SUMMARY AND CONCLUSIONS

We have provided a concise picture of NMR features for $BaFe_2Al_9$, giving a microscopic viewpoint for the change of the structural and electronic properties along with the phase transition. Distinctive features in the ^{27}Al NMR resonance lines, isotropic and anisotropic Knight shifts, as well as the spin-lattice relaxation rate have been characterized. A larger anisotropic Knight shift occurring at the Al(1) site indicates strong hybridization at this site, and the large EFG confirms the strong *ab* plane bonding configuration, providing a qualitative realization of the poor ductility in $BaFe_2Al_9$. The isotropic Knight shift together with the spin-lattice relaxation rate give a reasonable estimate of the Al-*s* $N_s(E_F)$ and an indication of orbital weights. We have further identified a substantial reduction in $N_s(E_F)$ at low temperatures, showing evidence for the Fermi-surface reconstruction accompanied by the phase transition for $BaFe_2Al_9$.

ACKNOWLEDGMENTS

This work is supported by the National Science and Technology Council of Taiwan under Grants No. 109-2112-M-006-013, No. 110-2124-M-006-006, and No. 110-2124-M-006-010. The authors are grateful to L. J. Chang of National Chen Kung University for the help with operating the Laue diffraction spectrometer. We gratefully acknowledge M. K. Lee for the magnetic susceptibility measurement. We also thank S. Y. Sun for the help with performing the NMR spectroscopy measurement at the Core Facility Center of National Cheng Kung University under Grant No. 110-2731-M-006-001.

[1] W. R. Meier, B. C. Chakoumakos, S. Okamoto, M. A. McGuire, R. P. Hermann, G. D. Samolyuk, S. Gao, Q. Zhang, M. B. Stone, A. D. Christianson, and B. C. Sales, Chem. Mater. **33**, 2855 (2021).

[2] C. S. Lue, Y.-K. Kuo, F. H. Hsu, H. H. Li, H. D. Yang, P. S. Fodor, and L. E. Wenger, Phys. Rev. B **66**, 033101 (2002).

[3] Y. Singh, D. Pal, S. Ramakrishnan, A. M. Awasthi, and S. K. Malik, Phys. Rev. B **71**, 045109 (2005).

[4] N. S. Sangeetha, A. Thamizhavel, C. V. Tomy, S. Basu, A. M. Awasthi, P. Rajak, S. Bhattacharyya, S. Ramakrishnan, and D. Pal, Phys. Rev. B **91**, 205131 (2015).

[5] B. R. Ortiz, S. M.L. Teicher, Y. Hu, J. L. Zuo, P. M. Sarte, E. C. Schueller, A. M. Milinda Abeykoon, M. J. Krogstad, S. Rosenkranz, R. Osborn, R. Seshadri, L. Balents, J. He, and S. D. Wilson, Phys. Rev. Lett. **125**, 247002 (2020).

[6] F. H. Yu, T. Wu, Z. Y. Wang, B. Lei, W. Z. Zhuo, J. J. Ying, and X. H. Chen, Phys. Rev. B **104**, L041103 (2021).
[7] K. Turban and H. Schäfer, J. Less-Common Met. **40**, 91 (1975).
[8] G. V. Vajenine and R. Hoffmann, J. Am. Chem. Soc. **120**, 4200 (1998).
[9] Z. Ryzynska, T. Klimczuk, and M. J. Winiarski, J. Solid State Chem. **289**, 121509 (2020).
[10] C. S. Lue, S. Chepin, J. Chepin, and J. H. Ross Jr., Phys. Rev. B **57**, 7010 (1998).
[11] T. J. Bastow, C. T. Forwood, M. A. Gibson, and M. E. Smith, Phys. Rev. B **58**, 2988 (1998).
[12] C. S. Lue, B. X. Xie, S. N. Horng, J. H. Su, and J. Y. Lin, Phys. Rev. B **71**, 195104 (2005).
[13] Y. Wang, X. Xi, Z. Li, E. Liu, Y. Yu, Y. Wu, G. Wu, and W. Wang, New J. Phys. **20**, 073026 (2018).
[14] C. S. Lue, T. H. Su, B. X. Xie, and C. Cheng, Phys. Rev. B **74**, 094101 (2006).
[15] C. S. Lue, R. F. Liu, Y. F. Fu, C. Cheng, and H. D. Yang, Phys. Rev. B **77**, 115130 (2008).
[16] S. Kawasaki, Y. Tani, T. Mabuchi, K. Kudo, Y. Nishikubo, D. Mitsuoka, M. Nohara, and G. Q. Zheng, Phys. Rev. B **91**, 060510(R) (2015).
[17] S. C. Chen and C. S. Lue, Phys. Rev. B **81**, 075113 (2010).
[18] C. S. Lue, S. H. Yang, T. H. Su, and B.-L. Young, Phys. Rev. B **82**, 195129 (2010).
[19] C. Benndorf, H. Eckert, and O. Janka, Acc. Chem. Res. **50**, 1459 (2017).
[20] C. Benndorf, O. Niehaus, H. Eckert, and O. Janka, Z. Anorg. Allg. Chem. **641**, 168 (2015).
[21] C. N. Kuo, C. W. Tseng, C. M. Wang, C. Y. Wang, Y. R. Chen, L. M. Wang, C. F. Lin, K. K. Wu, Y. K. Kuo, and C. S. Lue, Phys. Rev. B **91**, 165141 (2015).
[22] J. Shi and J. H. Ross Jr., Phys. Rev. B **45**, 8942 (1992).
[23] J. Shi, J. Chepin, and J. H. Ross Jr., Phys. Rev. Lett. **69**, 2106 (1992).
[24] K. Ghoshray, B. Pahari, A. Ghoshray, V. V. Eremenko, V. A. Sirenko, and B. H. Suits, J. Phys.: Condens. Matter **21**, 155701 (2009).
[25] S. Maeda, K. Matano, R. Yatagai, T. Oguchi, and G. Q. Zheng, Phys. Rev. B **91**, 174516 (2015).
[26] C. Mu, Q. Yin, Z. Tu, C. Gong, H. Lei, Z. Li, and J. Luo, Chin. Phys. Lett. **38**, 077402 (2021).
[27] S. Kawasaki, Z. Li, M. Kitahashi, C. T. Lin, P. L. Kuhns, A. P. Reyes, and Guo-qing Zheng, Nat. Commun. **8**, 1267 (2017).
[28] M. H. Cohen and F. Reif, *Solid State Physics* (Academic, New York, 1957), Vol. 5, p. 311.
[29] *Metallic Shifts in NMR*, edited by G. C. Carter, L. H. Bennett, and D. J. Kahan, (Pergamon, Oxford, 1977).
[30] A. R. Ferreira, J. Phys. Chem. C **123**, 9371 (2019).
[31] C. S. Lue and J. H. Ross Jr., Phys. Rev. B **60**, 8533 (1999).
[32] J. J. Spokas, C. H. Sowers, D. O. Van Ostenburg, and H. G. Hoeve, Phys. Rev. B **1**, 2523 (1970).
[33] J. Chi, Y. Li, F. G. Vagizov, V. Goruganti, and J. H. Ross Jr., Phys. Rev. B **71**, 024431 (2005).
[34] P. Jeglič, S. Vrtnik, M. Bobnar, M. Klanjšek, B. Bauer, P. Gille, Yu. Grin, F. Haarmann, and J. Dolinšek, Phys. Rev. B **82**, 104201 (2010).
[35] C. S. Lue, J. Y. Lin, and B. X. Xie, Phys. Rev. B **73**, 035125 (2006).
[36] A. M. Clogston, V. Jaccarino, and Y. Yafet, Phys. Rev. **134**, A650 (1964).
[37] A. Narath, Phys. Rev. **162**, 320 (1967).
[38] B. H. Suits and C. P. Slichter, Phys. Rev. B **29**, 41 (1984).
[39] H. F. Liu, C. N. Kuo, C. S. Lue, K.-Z. Syu, and Y. K. Kuo, Phys. Rev. B **88**, 115113 (2013).
[40] J. Korringa, Physica **16**, 601 (1950).
[41] C. S. Lue, B. X. Xie, and C. P. Fang, Phys. Rev. B **74**, 014505 (2006).
[42] C. P. Fang, C. S. Lue, and B. -L. Young, Phys. Rev. B **83**, 113105 (2011).
[43] C. W. Tseng, C. N. Kuo, H. W. Lee, K. F. Chen, R. C. Huang, C.-M. Wei, Y. K. Kuo, and C. S. Lue, Phys. Rev. B **96**, 125106 (2017).